Automatic Detection of Volcanic Unrest Using Blind Source Separation With a Minimum Spanning Tree Based Stability Analysis

Binayak Ghosh, Mahdi Motagh, Mahmud Haghshenas Haghighi, Magdalena Stefanova Vassileva, Thomas R. Walter, and Setareh Maghsudi

***Abstract*—Repeated synthetic aperture radar (SAR) acquisitions can be utilized to produce measurements of ground deformations and associated geohazards, such as it can be used to detect signs of volcanic unrest. Existing time series algorithms like permanent scatterer analysis and small baseline subset are computationally demanding and cannot be applied in near real time to detect subtle, transient, and precursory deformations. To overcome this problem, we have adapted a minimum spanning tree based spatial independent component analysis method to automatically detect sources related to volcanic unrest from a time series of differential interferograms. For a synthetic dataset, we first utilize the algorithm's capability to isolate signals of geophysical interest from atmospheric artifacts, topography, and other noise signals, before monitoring the evolution of these signals through time in order to detect the onset of a period of volcanic unrest, in near real time. In this article, we first demonstrate our approach on synthetic datasets having different signal strengths and temporal complexities. Second, we demonstrate our approach on a couple of real datasets, one acquired in 2017–2019 over the Colima volcano, Mexico, showing the occurrence of previously unrecognized short-term deformation events and the other over Mt. Thorbjorn in Iceland acquired over 2020. This shows the strength of the deep learning application to differential interferometric SAR measurements, and highlights that deformation events occurring without eruptions, which may have previously been undetected.**

***Index Terms*—Colima volcano, independent component analysis (ICA), Iceland, interferometric synthetic aperture radar (InSAR), Mexico, minimum spanning tree, MtThorbjorn, sentinel-1, volcano.**

Manuscript received May 5, 2021; revised June 14, 2021; accepted July 1, 2021. Date of publication July 19, 2021; date of current version August 18, 2021. This work was supported by the HEIBRiDS Research School (https://www.heibrids.berlin/) and in part by the Helmholtz Incubator Pilot Project TECVOLSA. *(Corresponding author: Binayak Ghosh.)*

Binayak Ghosh is with the GFZ German Research Centre for Geosciences, Technical University Berlin, 10623 Berlin, Germany (e-mail: binghosh@gmail.com).

Mahdi Motagh is with the GFZ German Research Centre for Geosciences, Institut für Photogrammetrie und GeoInformation, Leibniz Universität Hannover, 30167 Hannover, Germany (e-mail: motagh@gfz-potsdam.de).

Mahmud Haghshenas Haghighi is with the Institut für Photogrammetrie und GeoInformation, Leibniz Universität Hannover, 30167 Hannover, Germany (e-mail: mahmud@ipi.uni-hannover.de).

Magdalena Stefanova Vassileva and Thomas R. Walter are with the GFZ German Research Centre for Geosciences, 14473 Potsdam, Germany (e-mail: magda88@gfz-potsdam.de; twalter@gfz-potsdam.de).

Setareh Maghsudi is with the Eberhard Karl University of Tübingen, 72074 Tübingen, Germany (e-mail: maghsudi.setareh@uni-tuebingen.de).

Digital Object Identifier 10.1109/JSTARS.2021.3097895

I. Introduction

SURFACE deformation is one of the key parameters used for monitoring volcanoes and forecasting eruptions, realized by ground truthing and satellite remote sensing [1]. Over the years, various satellites like ERS-1, ERS-2, and Envisat have been in use for the interferometric capability for a wide range of geophysical [2]– [4] and environmental [5], [6] applications. Utilizing these synthetic aperture radar (SAR) acquisitions, repeated approximately from the same point in space at different times, interferometric SAR (InSAR) gives us the differences in path length in the scale of the carrier wavelength, due to changes in wavelength [7], [8]. While conventional InSAR suffers from interference from unwanted signals like variations of scattering properties of the earth's surface or atmospheric conditions through time [9], multitemporal interferometric methods including persistent scatter InSAR [10], [11], and small baseline subset (SBAS) [12] present a specific class of processing that exploits multiple SAR images acquired over an area to separate the displacement signal from the unwanted noise. The techniques are widely used by scientific communities to investigate surface deformations related to a broad range of geophysical [13]– [15] and engineering [16], [17] applications. To understand faults, volcanoes and ground stability, InSAR and time series analysis have grown from opportunistic science to routine monitoring techniques [18]. Nevertheless, due to the sheer number of data and targets, scientists, and operators are commonly focusing on large-scale and lasting unrest, while short-term deformation events may remain unexplored, however.

Displacement monitoring using advanced InSAR time series analysis methods has became standard at many observatories and potential sites of geohazards in recent years, where even large-scale products become available nationwide [19]. With the launches of Sentinel-1A and 1B satellites in 2014 and 2016, respectively, and the freely downloadable availability of SAR data from every part of the world, the methods application examples have been increased many folds. With short revisit times of 1–6 days, the Sentinel-1 and forthcoming missions provide an unprecedented wealth of topography monitoring and surface change data using the InSAR technique. With both Sentinel-1A and Sentinel-1B in orbit, this mission currently provides more than 10 TB [20] of products every day. Based on its acquisition plans, SAR images from the same orbit are acquired every 6 days

This work is licensed under a Creative Commons Attribution 4.0 License. For more information, see https://creativecommons.org/licenses/by/4.0/

over Europe as well as some hotspots with very rapid changes like Greenland [19]. In other parts of the world, SAR data are acquired every 12 or 24 days.

Instrumental data used for monitoring ground deformation is essential, allowing displacement detection at a millimeter-to-centimeter scale, but due to the difficult access and cost-effectiveness remote sensing is becoming an even broader standard, now covering even more volcanoes than those instrumentally monitored alone (e.g., [21], [22]. This has led to improvements in both, understanding and forecasting of volcanic eruptions [23]. InSAR algorithms like permanent scatterer (PS) and SBAS have proven to be effective in producing measurements of ground deformations that are easily interpretable to the human observer. However, one of the main problems while applying these algorithms for detecting signals of volcanic unrest is that they are computationally extensive and cannot be applied in real time to detect precursory deformation and transient deformations.

Machine learning technologies may contribute to the analysis of InSAR data, and already have been widely implemented in the field of computer science, where the computers use statistical techniques to learn a specific and complex task from given data. In the earth sciences, machine learning has been employed in several applications [24], such as predicting earthquake magnitudes [25], land surface classification [26], vegetation indices [27], or landslide susceptibility mapping [28].

Some of the previous works that have dealt with the application of machine learning technologies for the identification and classification of volcanic deformation include convolutional neural networks to automatically classify volcanic ground deformation from InSAR images [29]. The use of blind signal separation methods with InSAR data was demonstrated to be used in a simple detection algorithm [30]. The spatial independent component analysis (sICA) was applied to Sentinel-1 data and three signals were able to be isolated, which were of geophysical interest. The subsequent work [31] delves deeper into this method and investigates the reliability of the sources recovered by the independent component analysis (ICA) algorithm. The article adapts the ICASSO algorithm by [32] for isolating the latent sources. ICASSO runs an ICA algorithm several times and clusters estimated components from all runs based on the absolute value of the correlation between estimates, and then selects the centrotype of each cluster as the best estimate. However, the direct use of centrotypes can lead to loss of information, since more than one type of component may be grouped into the same cluster, but only one type of component can be selected as the centrotype, especially when the ICA model order is high [33]. Also, ICASSO can result in different runs selected for different components, which breaks the connection with the ICA mixing model.

In this article, to overcome these problems of conventional InSAR analysis and signal identification, we adapt a minimum spanning tree (MST) based approach [33] to investigate the stability of ICA algorithms for the extraction of latent signals from interferograms. This method is demonstrated for the Colima volcano in Mexico and Mt. Thorbjorn in Iceland, which are two of the most active volcanoes on Earth, and allows detecting previously unrecognized deformation events.

In this article, we first introduce the methods, by providing details on the developed algorithm and present the approach that uses a linear assignment problem and MST to solve the component sorting issue of the ICA algorithm. Then, we show results of a synthetic simulation test, as well as the results using real datasets from the Colima volcano in Mexico from 2017 to 2019 and another dataset from Mt. Thorbjorn in 2020. We discuss the advantages and limits of our approach and possible implications for volcano monitoring in general and the Colima volcano and Mt. Thorbjorn volcanoes in specific.

II. Method

A. Blind Signal Separation

Our method of automatic detection and extraction of geophysical signals from interferograms is following a three-step logic. The first step II-A1 uses multiple runs of a FastICA algorithm, inspired by the work by [31] to isolate the signals from a time series of interferograms. The second step II-A2 utilizes a linear assignment problem to find the best solution of sorting or ordering the estimated components, learned in the first stage for multiple runs. The third step II-A3 aims to select the best run out of the multiple runs, based on statistical significance, characterized by T-maps. These three steps are discussed in more details in the following sections.

We initially consider a dataset of interferograms having different values of temporal baseline. We then divide it into separate sections, each having a "daisy-chain" [34] of interferograms with same temporal baseline for each section.

1) Independent Component Analysis of Interferograms: The value of the independent component analysis for InSAR data analysis was recognized before [31]. Interferograms can be considered as a mixture of signals and with multiple latent signals combined in unknown quantities in an interferogram, recovering the original signals can be viewed as a problem of blind signal separation [30]. The ICA analysis of InSAR data, based on the prevalent literature [33], can be expressed as $X = A.S$ where $S=[s_1,...s_N]^T$ is an N-by-V source matrix, N is the number of sources, V is the number of pixels and s_i is the *i*th underlying component. The mixing matrix A is an M-by-N matrix where each column a_i represents the time course for the *i*th source. The goal of the algorithm is to determine the demixing matrix W such that the sources can be estimated using $S' = W.X$, assuming statistical independence of spatial components.

An ICA analysis approach [35] reshapes the interferograms such that the spatial dimension is treated as a single dimension and the individual intereferograms are concatenated in time. Then, a principal component analysis is applied to reduce the data dimension and then a FastICA decomposition is performed on the final matrix and individual interferograms are back reconstructed after this step. The entire algorithm is visually summarized in the Fig. 1 [33].

2) Linear Assignment Problem: In ICA algorithms, some components may be estimated inconsistently and slightly different components may be estimated during different runs. So,

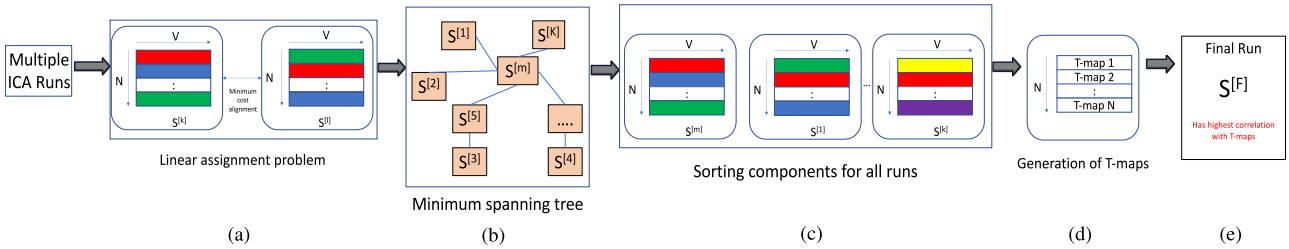

Fig. 1. Illustration of the MST-based ICA algorithm. (a) Multiple independent ICA runs are aligned and (b) formed into an MST, (c) all sources from other runs are aligned to the central run of the MST and (d) T-maps are generated for each cluster of components, (e) the final, most stable, is the run with highest average correlation to the group T-maps. [33].

the aim is to find the best sorting or ordering of the components for multiple runs.

In this article, we consider this problem as generalized assignment problem as stated in the article [33]. In a linear assignment problem (LAP) [36], 'given an equal number of agents and tasks, the idea is to assign each agent to exactly one task in such a manner that the overall cost of assignment is minimized.' The minimum cost and corresponding assignment for the ICA runs are obtained by applying Hungarian algorithm [37].

N independent components (ICs) are estimated from each ICA run. Then, an N-by-N matrix C_{mn} is calculated, which is the input cost of the LAP for sorting the *m*th and *n*th runs, where we consider c_{ij} = i-d($s_i^m s_j^n$) is the *ij*th entry of C_{mn}, s_i^m, and s_j^n are the ICs from the *m*th and *n*th runs, i,j [1,N], m,n [1,K], and d is the correlation coefficient. The minimum cost and corresponding assignment for each pair of ICA runs are obtained by applying the Hungarian algorithm. Then, an unconnected, undirected graph that includes K nodes (runs) and weighted edges having the minimum cost of LAP for each pair of ICA runs as weights. Next, an MST is calculated by finding a minimum-cost subgraph connecting all nodes [38]. Finally, the components in each run are reordered according to the central run in the obtained tree. The central run has the most connections with other runs and the minimum cost to the connected runs if there exists several runs having the same number of neighbors.

3) Best Run Selection Based on Statistical Significance: After the alignment of all the ICs from all runs is complete, one sample T-tests for each component estimate across K runs are performed to investigate the reliability of the ICA algorithm. Total of N T-maps, representing components across multiple runs are obtained. The best run is selected as the run with the highest correlation between estimated components and the corresponding T-maps. Thus, in this method, the consistently estimated components are favored when selecting the best run using T-maps [33].

For a given component, the average correlation, which is between the T-map and the same components from all runs, also represents the consistency of this component estimated by an ICA algorithm. For one run, the average correlation, which is between T-maps and the corresponding estimated components from this run, denotes the reliability of this ICA run based on statistical significance. We select the run having the highest reliability as the best run to perform subsequent analysis of the InSAR data.

4) Choice of Optimum Number of Sources to Extract: After the best run has been selected, the source matrix S, with the individual sources and the mixing matrix A, with the strengths of the individual source signals are retrieved. For each row of A, we can obtain the strength of the corresponding source over the time series. We can then extract the corresponding sources for each interferogram by simple dot product of the matrix A[i].S[i], where i is the *i*th row of the matrices denoting the *i*th interferogram in the dataset. Also, we can reconstruct the entire interferogram by just multiplying the whole mixing matrix A with the source matrix S. After all the interferograms have been reconstructed, the reconstructed and the original inteferograms are compared and the average root-mean-squared error (RMSE) is calculated.

As mentioned by earlier workers [31], the choice of the number of components to recover with ICA when the number of latent sources is unknown remains a difficult problem. Previous studies [30] and [31] highlight that the ICASSO algorithm was set to recover around two sources more than present in the data, as this ensures that the majority of the signals of interest that may exist in lower-importance principal components are not discarded. Similar to the work done in [31], we also first set up our algorithm to recover around four sources initially. We then calculate the RMSE between the reconstructed and the original interferograms, and then repeat this step continually with higher number of sources to recover. Once we have the RMSE values for the cases with approximately 7 or 8 recovered sources, we then compare the RMSE values and choose the case with least RMSE value as the optimum number of sources to extract.

5) Isolating the Deformation Signal From the Extracted Sources: The extracted sources may comprise of other signals like turbulence, strong atmospheric signal, or some topography correlated signals along with the deformation signal. For isolating the deformation signal from the other nonsignificant signals, first the strengths of all the extracted sources are plotted in the time series. The cumulative strength of all the extracted sources are calculated by adding the individual strengths of each source. Note that only nonconsistent signals, such as turbulence, should show the signal strength with the opposite sign and cancel out in the cumulative strength. Thus, the source having the highest absolute cumulative strength is considered as the major deformation signal.

In some cases, there may be seasonal displacements that have the signal strength with opposite sign and cancel out in the

cumulative strength. In these cases, to verify the occurrence of the deformation signal, a residual approach is employed similar to the method explained in [31]. The rms of the residual between each interferogram and the reconstructed interferogram is obtained as well as the residual for each pixel at each time step is also calculated. Then, the RMS of the sum of the residuals calculated from each pixel is obtained, which is the cumulative residual. This is used to identify any false positives, which may be attributed to some strong atmospheric artefacts in a single acquisition. The interferograms before and after this image will have the signal strength with opposite sign and, thus, cancel out in the cumulative residual. The recurring signals, like topography correlated signals, are captured in the modeled components. The deformation signals will show up as a change of rate for the cumulative residual. For a strong atmospheric signal, there may be some jumps in the residual but the cumulative residual of the subsequent acquisition will drop down again. Thus, in this case, due to the calculation of pixel-based residuals in each interferogram separately, even seasonal displacement signals with opposite signs in consecutive acquisitions, can be identified.

III. Data

We elaborate three datasets, first a suite of synthetic InSAR data generated to explore, develop, and challenge the methods we use, second, an InSAR time series developed from high resolution spotlight TerraSAR-X acquisitions over Colima volcano, Mexico and third, another InSAR time series developed from Sentinel-1 acquisitions over Mt. Thorbjorn in Iceland.

Many volcanic eruptions are commonly preceded by periods of inflation resulting from magma chamber pressurization caused by magma intrusion. After an eruption the magma chamber deflates and ground surface subsides, which is known as the deflation period. Monitoring inflation and deflation periods provides important clues about the structure and the state of active volcanoes. Monitoring typical background surface deformation at volcanoes also helps to detect the first sign of increase in the level of volcano activity, seismic precursors, and magma ascent.

For simulation of the surface deformation of volcanoes, synthetic interferograms of volcanoes having different types of Mogi sources [39] are constructed using ascending SAR geometry. The Mogi sources are pressure point sources, which can be used to model the inflation of the magma reservoir to simulate the levels of volcano activities.

Three categories of Mogi sources were simulated: source with a constant strength (constant pressure), source with a temporally increasing strength (increasing with time pressure) and an episodic source. The constant source has a specific constant amplitude throughout the entire duration, the amplitude of temporally increasing source increases with time and the episodic source has a high amplitude for a brief period of time and then subsides abruptly, as shown in Fig. 2. All the Mogi sources have a span of 1000 days. The temporal nature of the three types of Mogi sources considered has been illustrated in the Fig. 3. The details of the Mogi sources have been described in Table I.

Along with these Mogi sources, a ramp source and a tropospheric noise source were also simulated, as shown in Fig. 4.

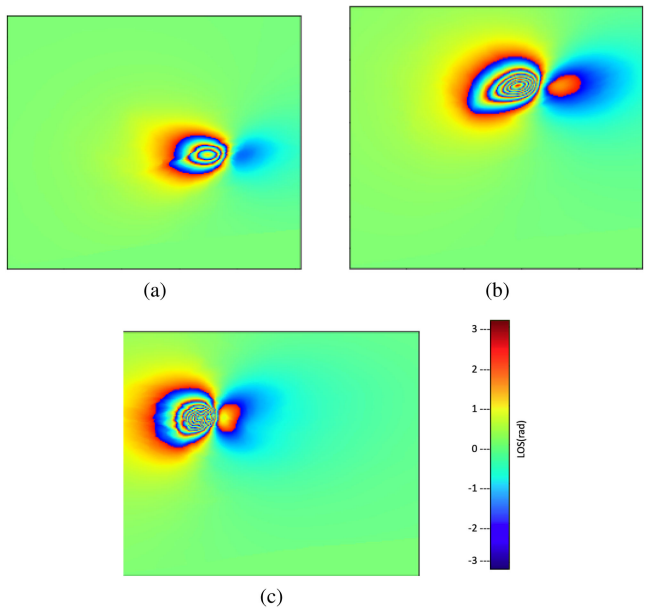

Fig. 2. Spatial orientation of three types of Mogi sources considered: (a) a constant source with a specific constant amplitude throughout entire duration, (b) a temporally increasing source, the amplitude of which increases with time, and (c) an episodic source which has a high amplitude for a brief period of time and then subsides abruptly.

TABLE I
Description of Mogi Sources

Mogi Source	Depth	Radius	Pressure
Constant Source	0.5 km	0.2 km	Day 0: 1e7 Pa; Day 1000: 1e7 Pa
Linearly increasing source	0.5 km	0.1 km	Day 0: 1e7 Pa; Day 1000: 5e8 Pa
Episodic source	0.5 km	0.2 km	Day 0: 0 Pa; Day 200: 3e7 Pa; Day 600: 3e7 Pa; Day 1000: 0 Pa

The ramp sources were constructed using this equation

$$\text{ramp} = b(1) + b(2) * \text{lon} + b(3) * \text{lat} + b(4) * \text{lon.} * \text{lat} + b(5) * \text{lon.}^2 + b(6) * \text{lat.}^2 \quad (1)$$

where b(i) are constants defined individually for each interferogram, lat and lon are latitute and longitude.The tropospheric phase is constructed assuming it has a linear correlation with topography with the equations

$$\text{dem} = (\text{dem} - \min(\text{dem}(:)))/(\max(\text{dem}(:)) - \min(\text{dem}(:))) \quad (2)$$

$$\text{ramp} = b(1) * \text{dem} \quad (3)$$

where b(1) is a constant, individually selected for each interferogram and dem is the digital elevation model. A normally distributed noise is added to each pixel phase.

Three different signal combinations have been used and three datasets having a combined total of 380 interferograms, characterized by 11, 22, and 33 days of temporal baseline, have been generated. In the first case, the interferograms were formed using only the episodic Mogi source, in the second case, all the Mogi sources were used and in the third case, all the Mogi sources

Fig. 3. Temporal nature of three types of Mogi sources considered for time ranges from T1 to T10. OS1, OS2, and OS3 refer to the three types of original Mogi sources: a constant source with a specific constant amplitude throughout entire duration, a temporally increasing source, the amplitude of which increases with time and an episodic source, which has a high amplitude for a brief period of time and then subsides abruptly, respectively.

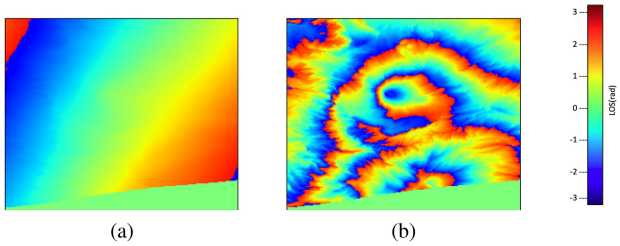

Fig. 4. (a) Ramp source, and (b) a tropospheric noise source.

as well as the ramp and tropospheric signals were combined together.

1) TerraSAR-X Data and Interferograms Over Colima Volcano: We used 82 SAR images acquired over Colima volcano by TerraSAR-X in spotlight mode. The data covers the period between 2017.01.08 and 2019.10.28. The revisit time of data is 11 days. However, it has several gaps. We selected the image acquired on 2018.05.07 as a reference. All other images are coregistered and resampled to the reference image. Then, we generated a network of interferograms with all possible image pairs. The topographic phase is compensated using a 7 m DEM generated from Pleiades optical images. An adaptive interferogram filtering is applied to the interferograms, and then, the interferograms are unwrapped.

1) Sentinel-1 Data and Interferograms Over Mt. Thorbjorn: We used 69 SAR images acquired over Mt. Thorbjorn. The data covers the period between 2019.11.09 and 2020.12.15. The revisit time of data is 6 days. However, it also has several gaps. We generated a network of interferograms with all possible image pairs. The topographic phase is compensated using ArticDEM of 2 m space resolution. An adaptive interferogram filtering is applied to the interferograms, and then, the interferograms are unwrapped.

IV. Results

A. Application to Synthetic Datasets

The algorithm was separately applied on each of the three synthetic datasets, having temporal baselines of 11, 22, and 33 days. For the first case, where only a single episodic Mogi source was considered without any ramp, troposphere or other signals, only one source was also recovered by the algorithm. The time series of the strength of the recovered source was plotted for each baseline in Fig. 5. As can be seen from the Fig. 5, the strength pattern clearly indicates that the amplitude of the source was initially close to 0, and then drastically increased to a certain value, which remained constant for a certain time, and then suddenly dropped back to near 0. This pattern clearly follows the episodic nature of the Mogi source that was used to simulate the interferograms.

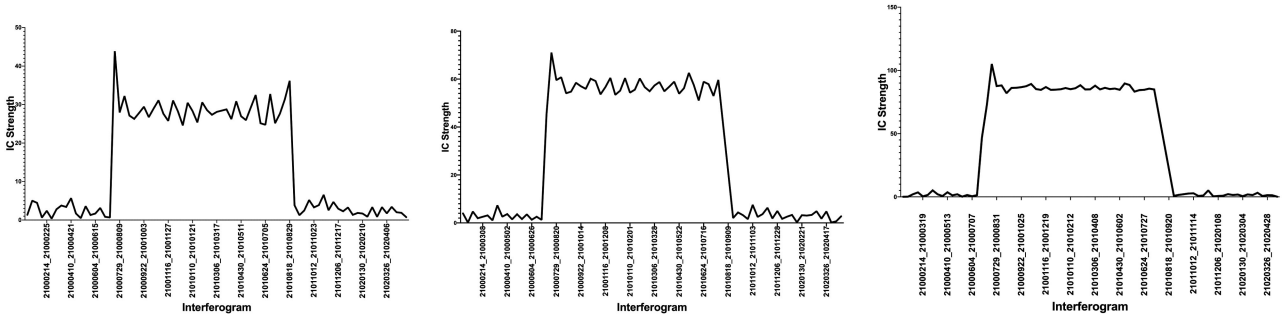

Fig. 5. Strengths of the recovered deformation source for temporal baseline of (a) 11, (b) 22, and (c) 33 days, respectively.

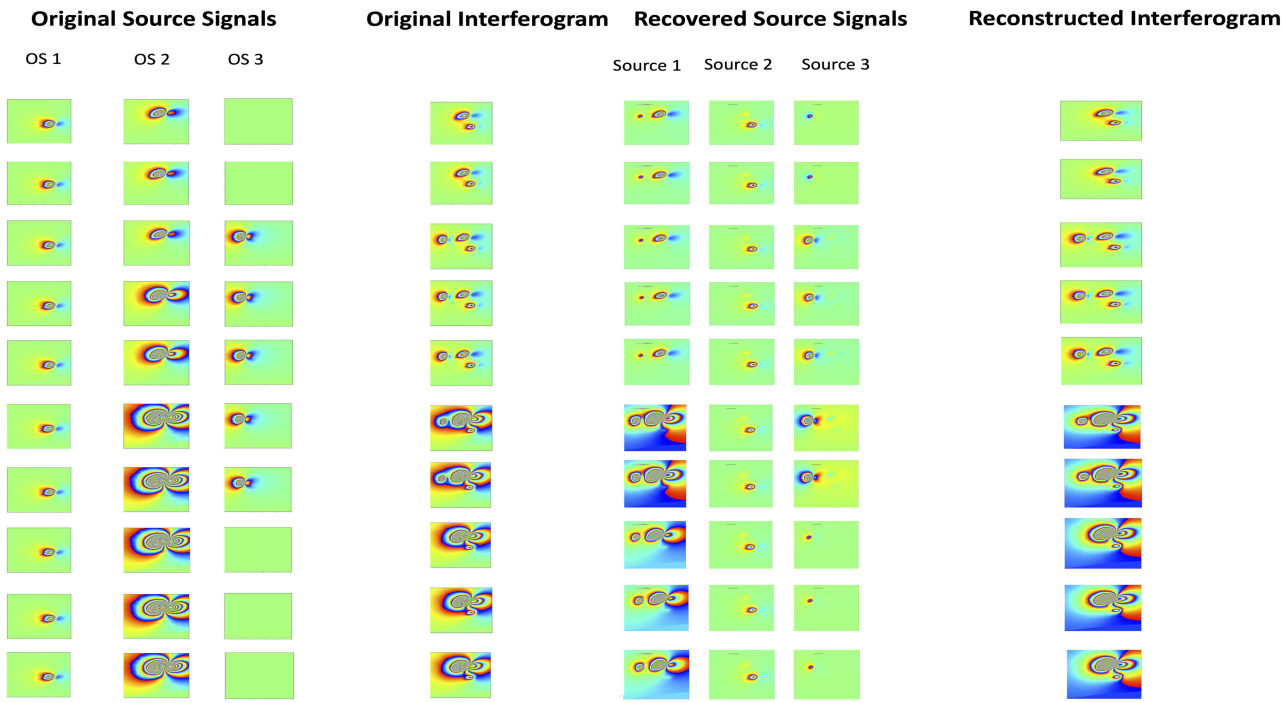

Fig. 6. Mogi source signals OS1, OS2, OS3, the original interferograms, the recovered signals from the algorithm and the reconstructed interferogram from the recovered signals for 10 different simulated interferograms.

For the second case, where all the Mogi sources were combined together, the algorithm was used to recover three different sources. The original and recovered sources are plotted in Fig. 6. The strengths of all the recovered sources were plotted, as shown in Fig. 8.

For the third case, where all the Mogi sources along with the ramp and tropospheric signals were combined together, the algorithm was used to recover four different sources. The number of sources to recover was based on the lowest MSE between the original interferogram and the reconstructed one, from the recovered sources, as mentioned in Section II-A4. The original and recovered sources are plotted in Fig. 7. The strengths of all the recovered sources were plotted for 11 days and 33 days temporal baselines, as shown in Fig. 8. In Fig. 8(b), it can be seen that, for 11 days, sources 1 and 2 remain constant for the entire duration of the time period and source 3 remains constant (almost 0) for some period of time, then increases with time and again stays constant for the rest for the time period, thus emulating the temporally increasing Mogi source. Source 4 was initially close to 0, and then increased to certain value, remained the same for some duration of time, and then finally dropped back to near 0 after some time, thus, clearly following the episodic Mogi source. In Fig. 8(c), for 33 days, a similar trend of the recovered sources are noticed. The results of this simulation, clearly indicate that the algorithm is able to distinguish between the different types of Mogi sources, of different strengths and different temporal nature and is able to recover these signals fruitfully, even when they are mixed with ramp, troposphere, and other noise signals.

B. *Application to the Volcán De Colima in Mexico*

The algorithm was applied on TerraSAR-X interferograms generated from the Volcán de Colima in Mexico. The considered

Fig. 7. Figure showing the Mogi source signals OS1, OS2, OS3, the ramp and tropospheric noise signals, the original interferograms, the recovered signals from the algorithm and the reconstructed interferogram from the recovered signals for 10 different simulated interferograms of temporal baseline 33 days.

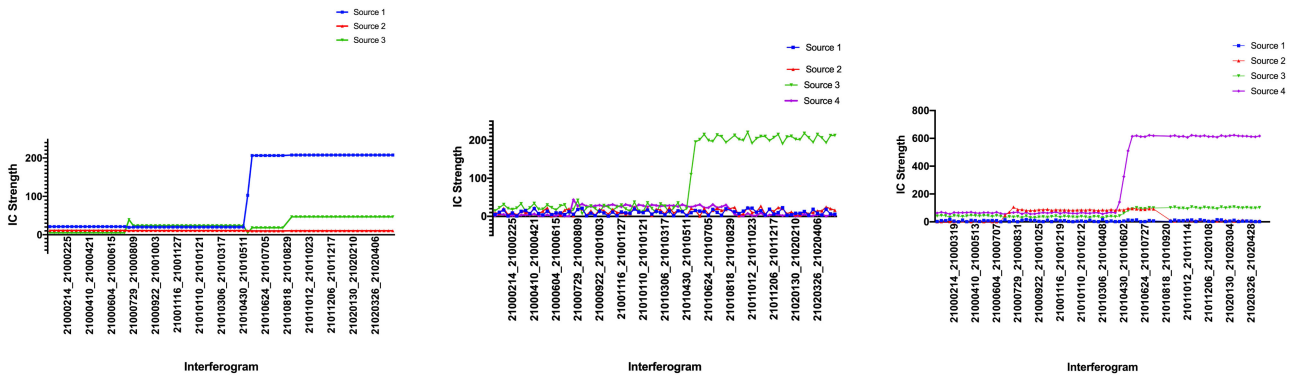

Fig. 8. (a) Strengths of the recovered sources for the second case with only the combination of the three Mogi sources, without any noise signal included. (b) and (c) Strengths of the recovered sources for the third case with the combination of the three Mogi sources as well as the noise signals included for temporal baseline of 11 and 33 days, respectively.

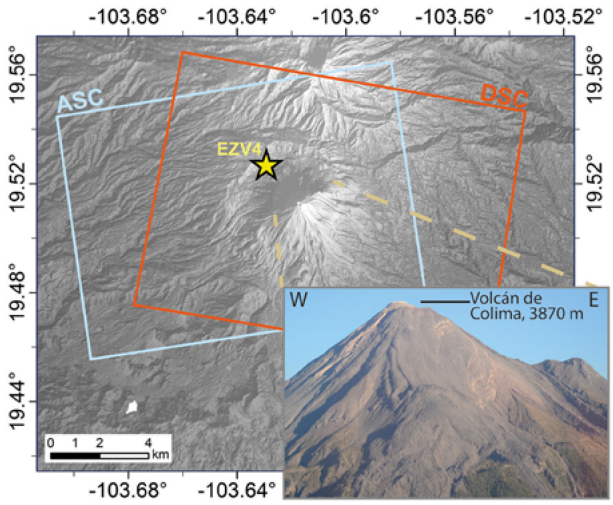

Fig. 9. Location map and overflight photograph of Volcán de Colima. The steep-sloped volcanic cone is approximately 4–6 km wide, and completely covered by both the ascending and descending TerraSAR-X satellite data (blue and red boxes in map view). The yellow star marks the seismic station EZV4 described in this article [44].

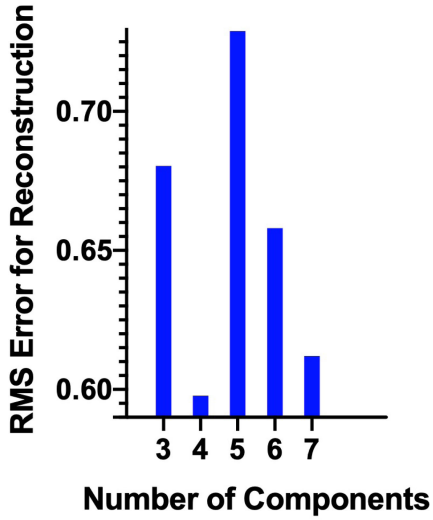

Fig. 10. Average rms error between original and reconstructed interferograms, for reconstruction based on 3, 4, 5, and 6 extracted sources. The minimum rms error was calculated for reconstruction with 4 extracted source signals.

time period from August 2017 to February 2018 is a intereruptive period, i.e., the volcano was in a state of relatively quiescence that was following a high intensity period that lasted from 2015 to 2017 [40].

Colima (19.514 N, 103.62 W, summit elevation 3850 m) (see Fig. 9 for location) has produced Plinian eruptions, pyroclastic flows, and large sector collapses in the past, and hosts a crustal reservoir at 12 km depth as well as shallower conduits or interfingered dykes [41]. The activity is characterized by a succession of eruptive cycles (dome construction followed by dome-destruction explosions and episodes of lava and/or pyroclastic flows) [42]. The volcano is located close to Colima town, a densely populated area with about 400 000 persons at risk, which is why understanding and monitoring the directions of dome growth and pyroclastic density currents is of vital interest [43]. The volcanic activity has been almost continuous since 1960 for Colima Volcano. Short-term inflation episodes precede sudden and explosive eruptions, such as on 6 January 2013, which are detected through synthetic aperture radar data [44]. The pre-eruptive inflation (updoming) of the summit region is inverted to a coeruptive deflation (subsidence) that can be described by a shallow spherical to elliptical pressure models [44], similar to the synthetic datasets we elaborated as described previously. Colima is a volcano challenging for ground truthing due to the hazardeous access to the summit, and challenging for InSAR studies due to signal decorrelation and geometric distortion [22].

On a report published in [45], it was mentioned that an eruptive episode began in January 2013 and continued through March 2017. In late April 2019, increased seismicity related to volcanic activity began again. This activity, through July 2019, is covered in [45]. The primary source of information was the Centro Universitario de Estudios e Investigaciones de Vulcanologia, Universidad de Colima.

Before applying the algorithm, the 200 interferograms were divided into three sets, of temporal baseline of 11, 33, and 44 days, respectively. The algorithm was applied to the three sets separately and the optimum number of sources to be recovered was determined by comparing the average MSE between the original and the reconstructed interferograms, for different number of recovered sources, as mentioned previously in Section II-A4. The optimum number of recovered sources were calculated to be 4 as outlined in the Fig. 10. Examples of the original and the reconstructed interferograms and the recovered sources are plotted in Fig. 11 for the three different baselines. For each of the three cases, the strengths of the recovered signals were plotted and as mentioned Section II-A5, the major deformation signals were isolated from all the recovered signals by calculating the absolute cumulative strength. Thus, sources 2, 1, and 4 were identified as the deformation signals for the set of interferograms having temporal baselines 11, 33, and 44 days, respectively. The absolute strengths of the deformation signals were then plotted in Fig. 12. As shown in Fig. 12, in all three cases strengths of the deformation signals showed a peak from March to April, November to December in 2017, and February to May in 2018, and February to July in 2019.

For isolating the periods of deformation from the time series of the strengths of the recovered deformation signals, a Z-score based outlier detection was performed for each of the time series for the different temporal baselines. For each time series, the Z-score of each point was calculated as the distance of the point from the mean value, in terms of the standard deviation. If the distance of the point from the mean was more than three times the standard deviation, the point was considered as an outlier, as shown in Fig. 12. The Z-score was calculated separately for each temporal baseline and, thus, for each time series for each temporal baseline, a distinct value of the Z-score was obtained. Taking the common time periods into consideration, the outliers or the peaks in the deformation signal strengths were

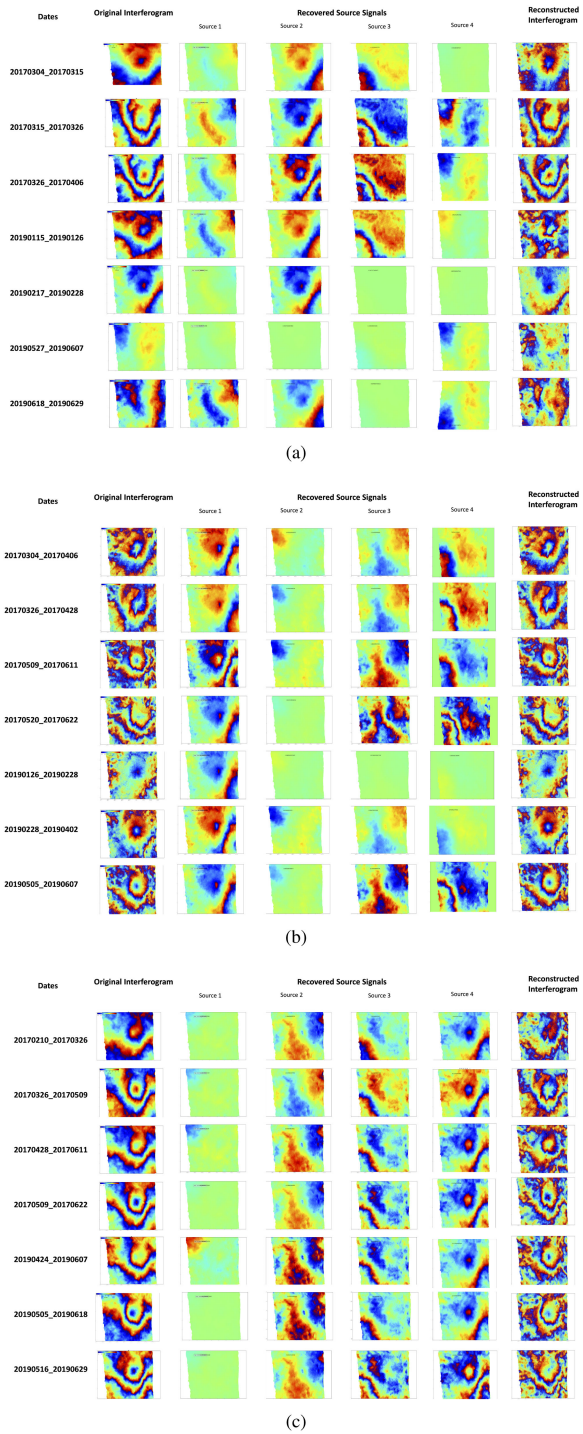

Fig. 11. Original interferograms, the recovered signals from the algorithm and the reconstructed interferogram from the recovered signals for 7 different interferograms of Volcan de Colima of temporal baseline (a) 11, (b) 33, and (c) 44 days.

found to be concentrated between March to April, November to December in 2017, and February to May in 2018, and February to July in 2019, as also mentioned previously. These periods of deformation are also corroborated by the times mentioned in the report [45], which stated that the seismicity related to volcanic activity continued around March 2017 and from April to July, 2019.

C. Application to Mt. Thorbjorn in Iceland

To demonstrate our automatic detection algorithm's ability to detect signs of volcanic unrest in real data, the algorithm was also applied on interferograms from Mt. Thorbjorn in Iceland, for the year 2020 and the results are presented here.

At the end of January 2020, a rapid, large-scale uplift accompanied by seismic swarms started to develop on the plate boundary of the Reykjanes Peninsula, in southwest Iceland (see Fig. 13, indicating a possible volcanic unrest and triggering a volcanic crisis in the region. Scientists and experts intensified the monitoring using ground and remote sensors in order to follow the evolution of the event. GPS and InSAR measurements, over the successive six months, detected three uplift episodes, each followed by light deflations, as shown in the Fig. 14. The center of the uplift, which remained stationary, was located about 1 km west of Mt. Thorbjörn. The maximum cumulative uplift was measured to be 12 cm. With good approximation, the inflation source was modeled as a Mogi point source.

InSAR time-series of Sentinel-1 data in ascending track has been processed for the period between November 2019 and December 2020 using 30 m of pixel size. Different time intervals have been used to create the interferograms: 6, 12, and 18 days. Specifically the uplift episodes correspond to the ascending Sentinel-1 data intervals: 20th January–19th February, 8th March–25th April, and 19th May–18th July.

Before applying the algorithm, the 200 interferograms were divided into three sets, of temporal baseline 6, 12, and 18 days, respectively. The algorithm was applied to the three sets separately and the optimum number of sources to be recovered was determined by comparing the average MSE between the original and the reconstructed interferograms, for different number of recovered sources, as mentioned in Section II-A4. The optimum number of recovered sources were calculated to be 4 as outlined in the Fig. 15. Examples of the original and the reconstructed interferograms and the recovered sources are plotted in the Fig. 16 for the three different baselines. For each of the three cases, the strengths of the recovered signals were plotted, and as mentioned in Section II-A5, the major deformation signals were isolated from all the recovered signals by calculating the absolute cumulative strength. Thus, sources 2, 4, and 3 were identified as the deformation signals for the set of interferograms having temporal baselines 6, 12, and 18 days, respectively. The absolute strengths of the deformation signals were then plotted in Fig. 17. As shown in Fig. 17, in all three cases, strengths of the deformation signals showed a peak from January to February and again from March to April.

For isolating the periods of deformation from the time series of the strengths of the recovered deformation signals, a Z-score based outlier detection was performed for each of the time series for the different temporal baselines, as before. Based on this analysis, the outliers or the peaks in the deformation signal strengths were found and highlighted are shown in the Fig. 17.

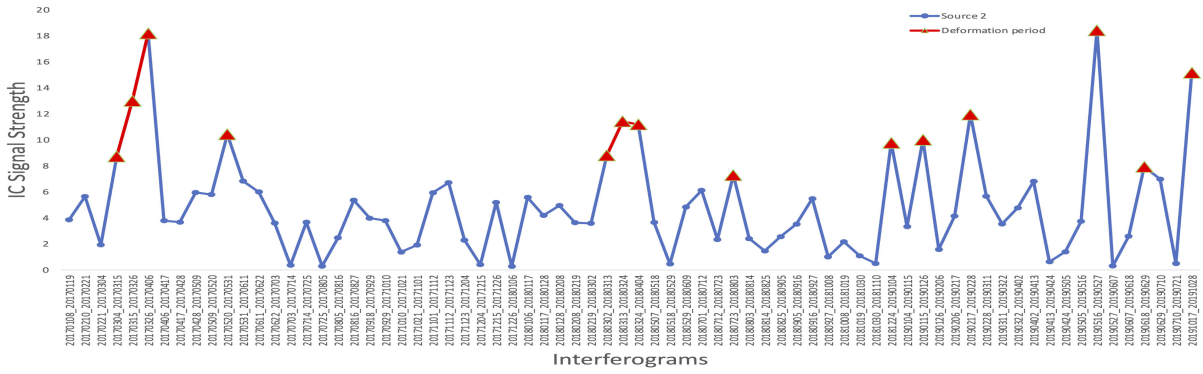

(a)

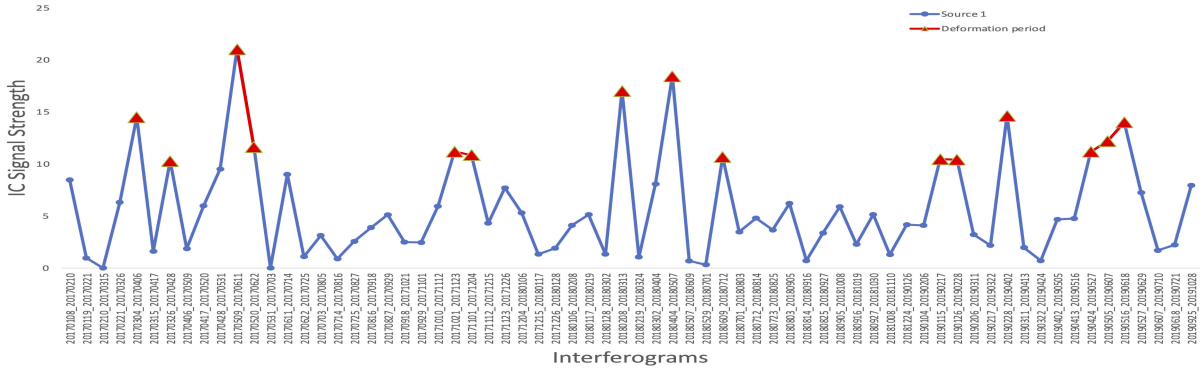

(b)

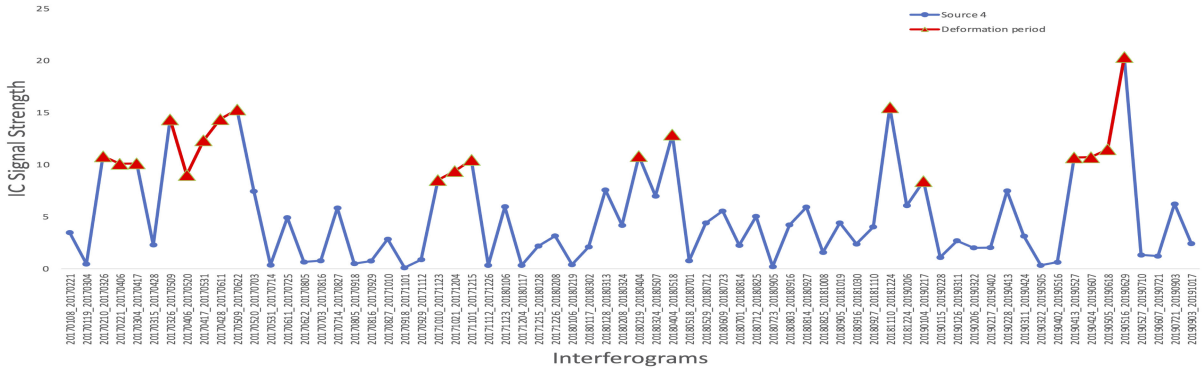

(c)

Fig. 12. Strengths of the recovered deformation sources for interferograms from the Volcán de Colima in Mexico from 2017 to 2019 with temporal baselines (a) 11, (b) 33, and (c) 44 days. The deformation periods as measured by the z-scores above the standard deviations have been highlighted. The z-score values are distinct for each time series with different temporal baseline.

The Z-score was calculated separately for each temporal baseline and, thus, for each time series for each temporal baseline, a distinct value of the Z-score was obtained. Taking the common time periods into consideration, the deformation signal peaks were found to be concentrated between January to February and again from March to April, as also mentioned previously. This is further corroborated if the time series of the strengths of the recovered deformation signals are compared to the LOS deformation (see Fig. 14 time series plot in the same region for the same time period. As shown in the Fig. 17, the uplift during the period of January to February and from March to April, as well as the rate of increase during these periods is in line with the peaks in the time series of the strengths of the recovered deformation signals during these time periods in the Fig. 14.

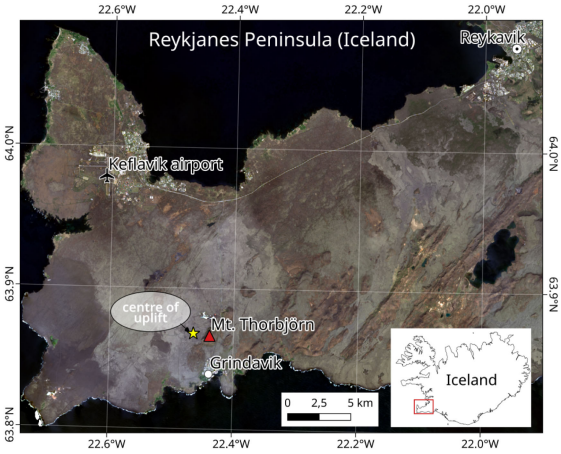

Fig. 13. Interferograms were formed Sentinel-1 SAR acquisitions of Mt. Thorbjorn in Iceland, covering dates from November 2019 to December 2020.

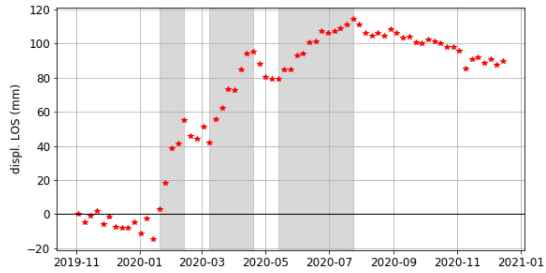

Fig. 14. GPS and InSAR measurements of Mt. Thorbjorn in Iceland, over the successive six months. Three uplift episodes were detected, each followed by light deflations.

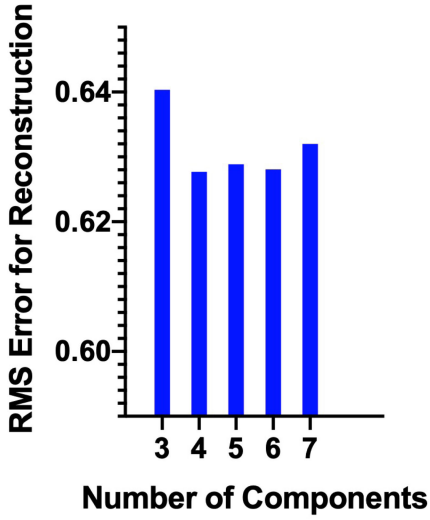

Fig. 15. Average rms error between original and reconstructed interferograms, for reconstruction based on 3, 4, 5, and 6 extracted sources. The minimum rms error was calculated for reconstruction with 4 extracted source signals.

The algorithm is computationally inexpensive, the interferometric phase data can be converted to a list of spatially independent sources and their associated time courses on a desktop or laptop computer in several minutes. New interferograms can also be added to this list in a few seconds. Therefore, this

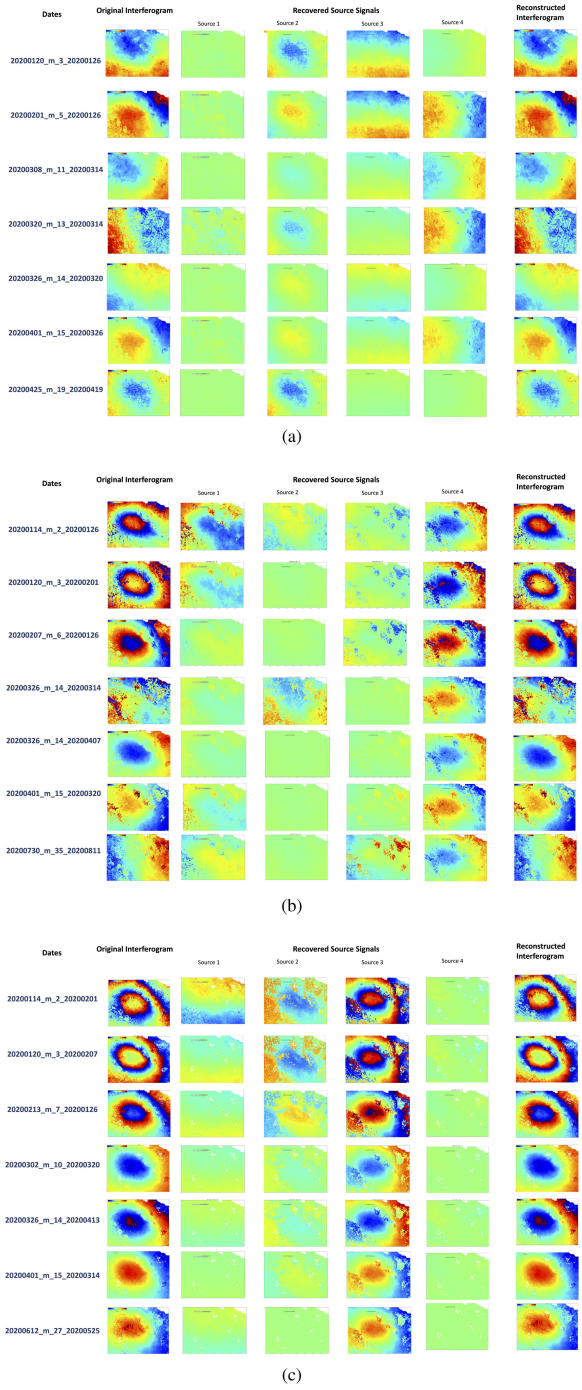

Fig. 16. Original interferograms, the recovered signals from the algorithm and the reconstructed interferogram from the recovered signals for 7 different interferograms of Mt. Thorbjorn of temporal baseline (a) 6, (b) 12, and (c) 18 days.

algorithm can be applied to Sentinel-1 data immediately upon being acquired to begin monitoring of the volcanic activity using interferograms.

V. Discussion

Volcano monitoring significantly contributes to forecasting and hazard assessment at active volcanoes. Deformation is a key

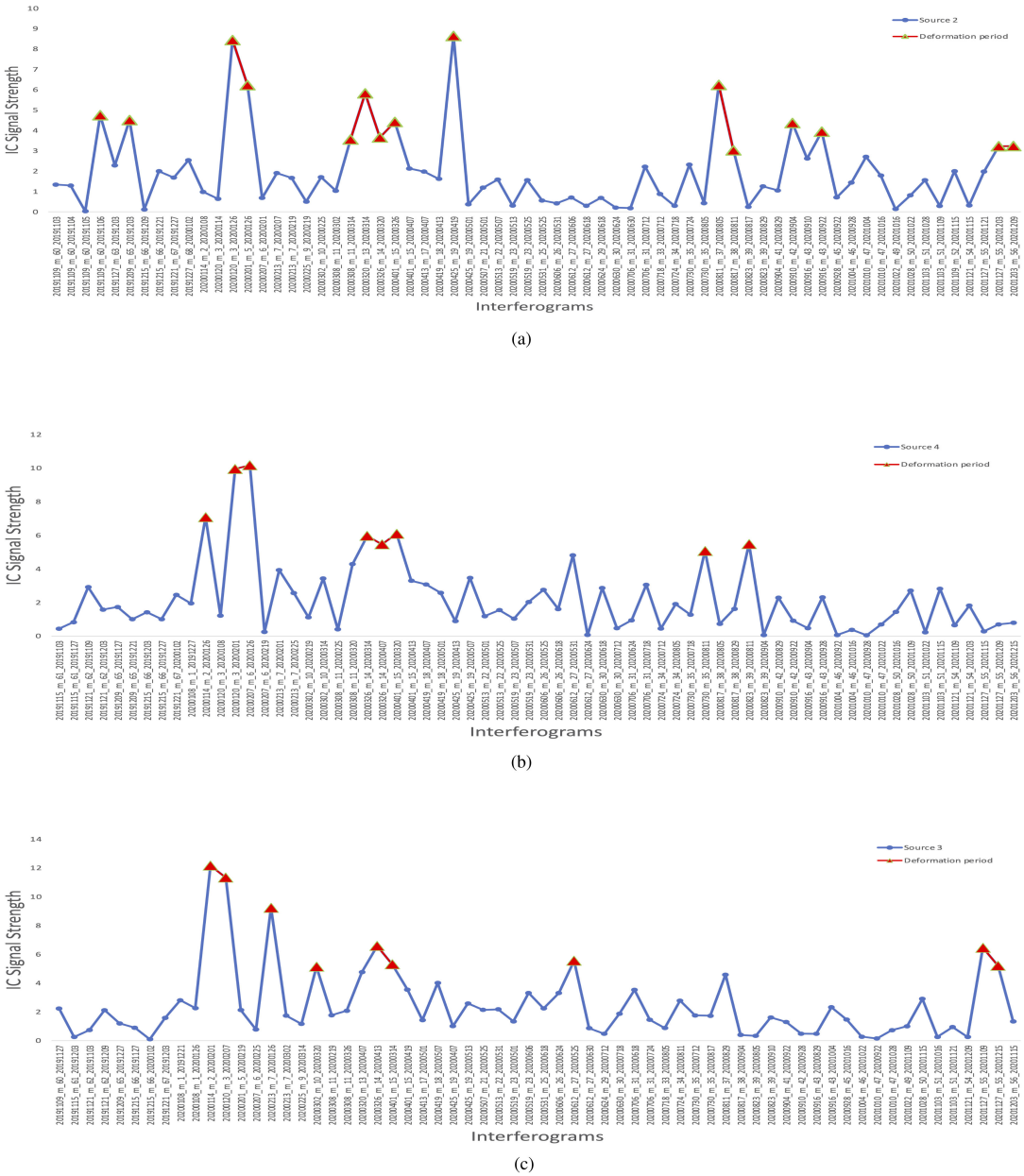

Fig. 17. Strengths of the recovered deformation sources for interferograms from Mt. Thorbjorn for 2020 with temporal baselines (a) 6, (b) 12, and (c) 18 days. The deformation periods as measured by the z-scores above the standard deviations have been highlighted. The z-score values are distinct for each time series with different temporal baseline.

parameter, besides seismicity, degassing, and temperature, that is monitored at volcanoes worldwide [1]. Comprehensive studies at over 500 volcanoes revealed that satellite remote sensing may greatly advance the deformation monitoring concept, with a high proportion of deforming volcanoes that also erupted [23]. A key challenge is that InSAR is still considered a postevent method that is mainly used for educational and research purposes applied for selected eruption periods, while numerous volcanoes show short deformation events without culminating in eruptions and remain detailed studies. With the advancement of automatic data acquisition and processing plans [46] monitoring of a much larger proportion of the 1500 active volcanoes worldwide becomes feasible, so that also the detection of noneruptive deformation events may sharply increase. To properly develop routines for monitoring and assessing the challenge of short-term deformation events, machine learning techniques may greatly contribute [29]–[31], [46].

A. *Automatic Signal Detection*

The minimum-spanning-tree based ICA algorithm can be applied to InSAR data for extracting sources of geophysical interest and for tracing strengths of the recovered deformation signals through time. In this article, a method for selecting the best ICA run out of multiple runs has been adapted from the paper [33]. Using assignment algorithm and MST, the sorting problem of

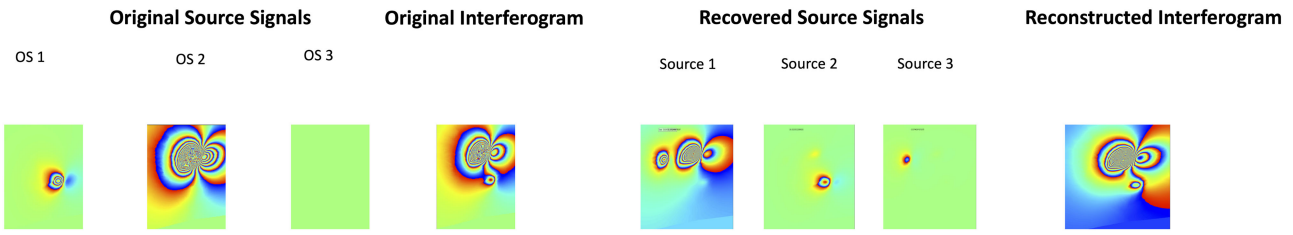

Fig. 18. Mogi source signals OS1, OS2, OS3, the original interferograms, the recovered signals from the algorithm and the reconstructed interferogram from the recovered signals a simulated interferogram.

different ICA runs has been addressed. This algorithm provides a way to select better ICA runs than the ICASSO algorithm and provides a more objective and better motivated approach to evaluate results. The utilization of the T-maps also provide a metric for interpreting the statistical reliability of estimated components for the given data.

The application of the algorithm on the simulated dataset has demonstrated its ability to detect changes in the most common types of Mogi sources, a constant, a temporally increasing and an episodic source strength, even when the multiple sources are combined together with noise signals to simulate real interferometric volcanic unrest signals. When the strengths of the detected deformation sources changes in rate, this is also detected by the algorithm, which gives us an idea of when volcanic inflation changes occurred.

The algorithm has proved effective in distinguishing the deformation signals from other extracted signals like turbulence, strong atmospheric signal, or some topography correlated signals as mentioned in the Section II-A5. Similarly, as mentioned in [31], false positives generated by strong atmospheric turbulence can be identified as false when the signal reverses in the subsequent image. Inspection of other acquisitions from a different geometry or satellite, prior to the subsequent image, could also be used to rule out deformation.

One of the drawbacks of the algorithm is the appearance of discrepancies while trying to extract multiple source signals, which are temporally as well as spatially correlated. In Fig. 18, it can be seen that, all three of the original Mogi sources OS1, OS2, and OS3 have considerable amplitude and are prevalent almost at the same point in time. So, while trying to extract the three sources separately from the original interferogram, some residual complimentary versions of one of the sources appear with the other sources. To illustrate this, in Fig. 18, a complimentary fraction of the Source 3 is prevalent in the recovered Source 1. The reason can be attributed to the fact that the ICA algorithm is able to distinguish between different sources based on the amplitudes. However, this distinction among separate signals is minimal on a spatial level, i.e., if the signals overlap on a common spatial position.

In this project, the method employed to mitigate the occurrence of these discrepancies is to check if there are complimentary pixel values at the same positions in the separate recovered sources and eliminate the complimentary versions as much as possible. This can work as a way to minimize the error occurring due to spatial overlap, but still in some cases, the residuals remain to a minimal extent.

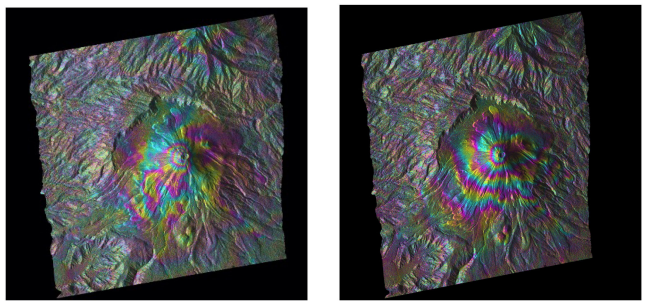

(a) (b)

Fig. 19. Differential TerraSAR-X interferogram over Volcan de Colima, Mexico for dates (a) 23.11.2017–04.12.2017 and (b) 04.04.2018–05.18.2018.

B. Volcanic Unrest Determination in Volcan De Colima, Mexico in 2017–2019

The presented algorithm was applied to model the unrest of Volcan de Colima in Mexico for the period of 2017 to 2019. The period investigated destruction of a summit lava dome during the period December 2016 to March 2017 [40]. As recorded by the local volcano observatory of Colima, only minor activity followed, the smaller degassing and explosion events during the years 2017–2018 are mostly monitored by the Red Sismológica Telemétrica del Estado de Colima of the volcano observatory, revealing short-term increased seismicity and changes from long-period to short-period events related to the volcanic activity [43] and continued until July 2019. For detecting both short and long term deformations over the period of three years, interferograms of short temporal baseline of 11 days, and interferograms of longer temporal baselines of 33 and 44 days were investigated. As shown in our results from the Section IV-B, the algorithm was able to recover deformation source events in March 2017 and April 2017, respectively, as well as others in February and July 2019. Besides that, other deformation episodes due to volcanic unrest were also detected in the periods from November to December in 2017 and from February to May in 2018. These unrest episodes were not documented in any literature, but barely recognized by observers of the volcano observatory (need to add a figure). While analyzing the interferograms from late 2017 to 2018, the fringes highlighting the deformations are clearly visible in the interferograms, as shown in the Fig. 19. One of the reasons that there is no documented version of these volcanic episodes from the Colima volcano can be attributed to the fact that these deformations were during a period, where the rate of seismicity was quite slow. Thus, these signals can only

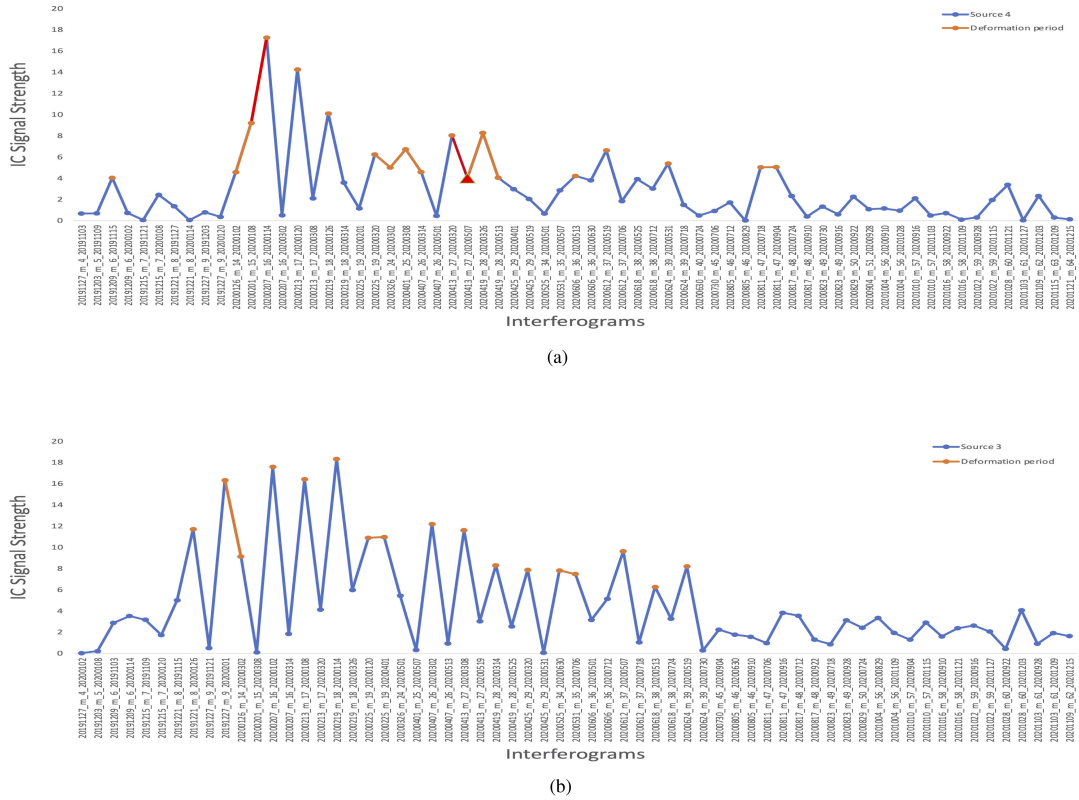

Fig. 20. Strengths of the recovered deformation sources for interferograms from Mt. Thorbjorn for 2020 with temporal baselines (a) 24 and (b) 36 days. The deformation periods as measured by the z-scores above the standard deviations have been highlighted. The z-score values are distinct for each time series with different temporal baseline.

be detected after analyzing intereferograms of long temporal baselines of around 44 days.

C. Volcanic Unrest Determination in Mt. Thorbjorn, Iceland in 2020

This algorithm was applied to model the volcanic unrest determination in Mt. Thorbjorn in Iceland throughout entire 2020. The volcanic source in this case study, can be approximated to a Mogi source with a cyclic increment strength. As shown in Fig. 14, the uplift episodes occurred in the date intervals: 20th January–19th February, 8th March–25th April, and 19th May–18th July. The strengths of the recovered deformation sources, as plotted in Fig. 17, show that the deformation signal strengths were also significantly high during the period of January to February and from March to April. Further inspection of the Fig. 14 showed that rate of uplift was lower in the period from May to July, compared to January-February and March-April. Since only the short-term interferograms of 6, 12, and 24 days were investigated, during the period from May to July the uplift signal was not strong enough to be well visible in such a short-term interferograms. For further investigation, the algorithm was applied to interferograms of the same region for temporal baselines of 36 and 44 days. The strengths of the deformation sources for the temporal baselines 36 and 44 days are plotted in the Fig. 20. As can be seen from the Fig. 20, the strengths of the deformation sources for both 24 and 36 days temporal baselines, show significant peaks during the period from May to July, apart from January-February and March-April. This validates the idea that the rate of uplift was lower during this period compared to January to March, and so these peaks are visible in interferograms of longer temporal baselines like 24 and 36 days.

One interesting part to note is that for both the Colima volcano as well as Mt. Thorbjorn, the number of components derived in both cases was four. This can be attributed to the fact that in both cases, the number of components derived is in agreement with the number of components in the actual data, which is also statistically verified when the RMSE is the least in both cases. If the number of components to be derived is considered higher or lower than four in both cases, then the derived components do no fit properly during the inversion. Regarding the geophysical interpretation, in both cases, the four derived sources comprise of the deformation source, the atmospheric artefacts, a topography related source and another source depicting the broad scale trend. Thus, in both cases, it can be seen, both statistically as well as geophysically that the optimum number of sources to isolate to obtain best result for inversion of the interferograms is 4.

VI. Conclusion

This article shows that the quality and interpretability of the extracted sources can be potentially enhanced by leveraging a more general ICA algorithm in combination with the MST-based stability analysis. This article has shown that this algorithm can be used to extract latent deformation sources from InSAR data

and it is able to detect signs of volcanic unrest due to both a change in a pre-existing signal as well as due to emergence of a new signal. It can be used as an automatic application for early warning of signs of volcanic unrest, when using interferograms of shorter temporal baselines. Along with that, it can also be used for long term deformation monitoring when interferograms of longer temporal baselines are taken into account.

In this article, this algorithm has been applied to a synthetic dataset of simulated Mogi sources, as well as two real datasets from Volcan de Colima in Mexico and from Mt. Thorbjorn in Iceland. The algorithm proved successful in extracting deformation events from the interferograms of varying temporal baselines. The time series of the strengths of the recovered deformation sources also provided an overview of how the deformation signals varied through time. The results show that it would have been possible to promptly and automatically (without the need of an expert data interpretation) flag a volcano as entering a period of increased activity when the strengths of the deformation source increased before an eventual eruption and so could have provided some warning that the volcano had entered a period of heightened unrest. Thus, it shows that this algorithm could be applied globally for any monitoring all types of volcanic unrest. Moreover, this article shows that deformation events occur at Colima, that are appearing without any eruption (e.g., add the dates of these events here). The pattern and strengths of these deformation events detected by our machine learning approach are comparable to those deformation events that immediately preceded explosive eruptions [44]. This bears potential for false alarms and highlights the need to better understand the episodes of uplift and subsidence of volcano summits.

VI. Author Contributions

Binayak Ghosh: Conceptualization, Methodology, Data processing, Formal analysis, Writing-original draft, Visualization. Mahdi Motagh: Conceptualization, Methodology, Writing-review and editing, Supervision. Mahmud Haghshenas Haghighi: Data Acquisition, Data Processing, Formal analysis. Magdalena Stefanova Vassileva: Data Acquisition, Data Processing, Formal analysis. Thomas R. Walter: Conceptualization, supervision, review and editing. Setareh Maghsudi: Conceptualization, supervision, review, and editing.

VI. Conflict of Interest Statement

The authors declare that they have no known competing financial interests or personal relationships that could have appeared to influence the work reported in this article.

Acknowledgment

The oroginal TerraSAR-X data (covering the Volcan de Colima, Mexico) are copyright of German Aerospace Agency (DLR). The original Copernicus Sentinel data (covering Mt. Thorbjorn, Iceland) are copyright of the European Space Agency and were obtained by the authors of this article from the Alaska Satellite Facility archive[1]. Figures were prepared in Matplotlib [47]. The graphs were plotted using Graphpad Prism [48] and Microsoft Excel [49].

[1][Online]. Available: https://www.asf.alaska.edu/

References

[1] D. Dzurisin, *Volcano Deformation: New Geodetic Monitoring Techniques (Geophysical Sciences)*. Berlin, Germany: Springer, 2007.

[2] J. Hole, C. Bromley, N. Stevens, and G. Wadgs, "Subsidence in the geothermal fields of the Taupo Volcanic Zone, New Zealand from 1996 to 2005 measured by InSAR," *Volcanol. Geotherm*, vol. 166, pp. 125–146, 2007.

[3] V. Kumar, G. Venkataraman, Y. Rao, G. Singh, and Snehamani, "Space-borne InSAR Technique for Study of Himalayan glaciers using ENVISAT ASAR and ERS data," in *Proc. IEEE Int. Geosci. Remote Sens. Symp.*, 2008, pp. IV-1085–IV-1088.

[4] M. Motagh *et al.*, "Land subsidence in Iran caused by widespread water reservoir overexploitation," *Geophys. Res. Lett*., vol. 35, 2008, Art. no. L16403.

[5] T. Castel, J.-M. Martinez, A. Beaudoin, U. Wegmüller, and T. Strozzi, "ERS INSAR data for remote sensing hilly forested areas," *Remote Sens. Environ*., vol. 73, pp. 73–86, 2000.

[6] M. Santoro, J. Askne, U. Wegmüller, and C. Werner, "Observations, modeling, and applications of ERS-ENVISAT coherence over land surfaces," *IEEE Trans. Geosci. Remote Sens*., vol. 45, no. 8, pp. 2600–2611, Aug. 2007.

[7] D. Massonnet and K. Feigl, "Radar interferometry and its application to changes in the earth's surface," *Rev. Geophys.*, vol. 36, no. 4, pp. 441–500, Nov. 1998.

[8] R. Bürgmann, P. Rosen, and E. Fieldling, "Synthetic aperture radar interferometry to measure earth's surface topography and its deformation," *Annu. Rev. Earth Planet. Sci*., vol. 28, pp. 169–209, 2008.

[9] A. Hooper, D. Bekaert, K. Spaans, and M. Ankan, "Recent advances in SAR interferometry time series analysis for measuring crustal deformation," *Tectonophysics*, vol. 514–517, pp. 1–13, 2012.

[10] A. Ferretti, C. Prati, and F. Rocca, "Permanent scatterers in SAR interferometry," *IEEE Trans. Geosci. Remote Sens*., vol. 39, no. 1, pp. 8–20, Jan. 2001.

[11] A. Hooper, H. Zebkar, P. Segall, and B. Kampes, "A new method for measuring deformation on volcanoes and other natural terrains using InSAR persistent scatterers," *Geophys. Res. Lett*., vol. 31, no. 23, Dec. 16, 2004.

[12] P. Berardino, G. Fornaro, R. Lanari, and E. Sansoti, "A new algorithm for surface deformation monitoring based on small baseline differential SAR interferograms," *IEEE Trans. Geosci. Remote Sens*. vol. 40, no. 11, pp. 2375–2383, Nov. 2002.

[13] A. Hooper, P. Segall, and H. Zebkar, "Persistent scatterer interferometric synthetic aperture radar for crustal deformation analysis, with application to Volcán Alcedo," *Galápagos. J. Geophys. Res. B Solid Earth*, vol. 112, 2007, Art. no. B07407.

[14] M. H. Haghighi and M. Motagh, "Assessment of ground surface displacement in Taihape Landslide, New Zealand, with C-and X-band SAR interferometry," New *Zeland J. Geol. Geophys*., vol. 59, pp. 136–146, 2016.

[15] M. Motagh *et al.*, "Quantifying groundwater exploitation induced subsidence in the Rafsanjan plain, southeastern Iran, using InSAR time-series and in situ measurements," *Eng. Geol*., vol. 218, pp. 134–151, 2017.

[16] G. Fornaro, D. Reale, and S. Verde, "Bridge thermal dilation monitoring with millimeter sensitivity via multidimensional SAR imaging," *IEEE Geosci. Remote Sens. Lett*. vol. 10, no. 4, pp. 677–681, Jul. 2013.

[17] L. Emadali, M. Motagh, and M. H.Haghighi, "Characterizing post-construction settlement of the Masjed-Soleyman embankment dam, southwest Iran, using TerraSAR-X SpotLight radar imagery," *Eng. Struct.,* vol. 143, pp. 261–273, 2017.

[18] J. Biggs and T. J. Wright, "How satellite InSAR has grown from opportunistic science to routine monitoring over the last decade," *Nat. Commun.*, vol. 11, no. 1, Aug. 2020, Art. no. 3863.

[19] M. H. Haghighi and M. Motagh, "Sentinel-1 InSAR over Germany: Large-scale interferometry, atmospheric effects, and ground deformation mapping," *ZFV - Zeitschrift fur Geodasie, Geoinformation und Land Manage.,* vol. 142, no. 4, pp. 245–246, Jan. 2017.

[20] *Sentinel Data Access Annual Report 2017*. 2017. [Online]. Available: https://sentinel.esa.int/web/sentinel/news/-/article/sentinel-data-access-annual-report-2017

[21] J. Biggs and M. E. Pritchard, "Global volcano monitoring: What does it mean when volcanoes deform?," *Elements*, vol. 13, no. 1, pp. 17–22, Feb. 2017.
[22] V. Pinel, A. Hooper, S. De la Cruz-Reyna, G. Reyes-Davila, M. P. Doin, and P. Bascou, "The challenging retrieval of the displacement field from InSAR data for andesitic stratovolcanoes: Case study of popocatepetl and Colima volcano, Mexico," *J. Volcanol. Geothermal Res.*, vol. 200, no. 1, pp. 49–61, Feb. 2011.
[23] J. Biggs *et al.*, "Global link between deformation and volcanic eruption quantified by satellite imagery," *Nat. Commun.*, vol. 5, no. 1, Apr. 2014, Art. no. 3417.
[24] D. J. Lary, A. H. Alavi, A. H. Gandomi, and A. L. Walker, "Machine learning in geosciences and remote sensing," *Geosci. Front.*, vol. 7, no. 1, pp. 3–10, Jan. 2016.
[25] H. Adeli and A. Panakkat, "A probabilistic neural network for earthquake magnitude prediction," *Neural Netw.*, vol. 22, no. 7, pp. 1018–1024, Sep. 2009.
[26] C. Li, J. Wang, L. Wang, L. Hu, and P. Gong, "Comparison of classification algorithms and training sample sizes in urban land classification with landsat thematic mapper imagery," *Remote Sens.*, vol. 6, no. 2, pp. 964–983, Feb. 2014.
[27] M. E. Brown, D. J. Lary, A. Vrieling, D. Stathakis, and H. Mussa, "Neural networks as a tool for constructing continuous NDVI time series from AVHRR and MODIS," *Int. J. Remote Sens.*, vol. 29, no. 24, pp. 7141–7158, Dec. 2008.
[28] I. Yilmaz, "Comparison of landslide susceptibility mapping methodologies for Koyulhisar, Turkey: Conditional probability, logistic regression, artificial neural networks, and support vector machine," *Environ. Earth Sci.*, vol. 61, no. 4, pp. 821–836, Aug. 2010.
[29] N. Anantrasirichai, J. Biggs, F. Albino, P. Hill, and D. Bull, "Application of machine learning to classification of volcanic deformation in routinely generated InSAR data," *J. Geophys. Res. Solid Earth*, vol. 123, no. 8, pp. 6592–6606, 2018.
[30] M. E. Gaddes, A. Hooper, M. Bagnardi, H. Inman, and F. Albino, "Blind signal separation methods for InSAR: The potential to automatically detect and monitor signals of volcanic deformation," *J. Geophys. Res. Solid Earth*, vol. 123, no. 11, pp. 10 226–10251, 2018.
[31] M. E. Gaddes, A. Hooper, and M. Bagnardi, "Using machine learning to automatically detect volcanic unrest in a time series of interferograms," *J. Geophys. Res. Solid Earth*, vol. 124, no. 11, pp. 12304–12322, 2019.
[32] J. Himberg, A. Hyvärinen, and F. Esposito, "Validating the independent components of neuroimaging time series via clustering and visualization," *NeuroImage*, vol. 22, no. 3, pp. 1214–1222, Jul. 2004.
[33] W. Du, S. Ma, G. Fu, V. D. Calhoun, and T. Adali, "A novel approach for assessing reliability of ICA for FMRI analysis," in *Proc. IEEE Int. Conf. Acoust. Speech Signal Process.*, 2014, pp. 2084–2088.
[34] J. Biggs, E. Y. Anthony, and C. J. Ebinger, "Multiple inflation and deflation events at Kenyan volcanoes, East African rift," *Geology*, vol. 37, no. 11, pp. 979–982, Nov. 2009.
[35] V. D. Calhoun, T. Adali, G. D. Pearlson, and J. J. Pekar, "A method for making group inferences from functional MRI data using independent component analysis," *Hum. Brain Mapping*, vol. 14, no. 3, pp. 140–151, Nov. 2001.
[36] T. C. Koopmans and M. Beckmann, "Assignment problems and the location of economic activities," *Econometrica*, vol. 25, no. 1, pp. 53–76, 1957.
[37] H. W. Kuhn, "The hungarian method for the assignment problem," *Nav. Res. Logistics Quart.*, vol. 2, no. 1/2, pp. 83–97, 1955.
[38] J. B. Kruskal, "On the shortest spanning subtree of a graph and the traveling salesman problem," *Proc. Amer. Math. Soc.*, vol. 7, no. 1, pp. 48–50, 1956.
[39] K. Mogi, "Relations between the eruptions of various volcanoes and the deformations of the ground surfaces around them," *Bull. Earthq. Res. Inst.*, vol. 36, pp. 99–134, 1958.
[40] R. Armbula-Mendoza *et al.*, "Destruction of a lava dome observed with photogrammetry, acoustic and seismic sensors at Volcn de Colima, Mexico," *J. Volcanol. Geothermal Res.*, vol. 395, Apr. 2020, Art. no. 106834.
[41] Z. Spica, M. Perton, and D. Legrand, "Anatomy of the Colima volcano magmatic system, Mexico," *Earth Planet. Sci. Lett.*, vol. 459, pp. 1–13, Feb. 2017.
[42] T. R. Walter *et al.*, "Imaging the 2013 explosive crater excavation and new dome formation at Volcan de Colima with TerraSAR-X, time-lapse cameras and modeling," *J. Volcanol. Geothermal Res.*, vol. 369, pp. 224–237, Jan. 2019.
[43] E. U. Zorn *et al.*, "Load stress controls on directional lava dome growth at Volcan de Colima, Mexico," *Front. Earth Sci.*, vol. 7, 2019, Art. no. 84.
[44] J. T. Salzer *et al.*, "Satellite radar data reveal short-term pre-explosive displacements and a complex conduit system at Volcn de Colima, Mexico," *Front. Earth Sci.*, vol. 2, 2014, Art. no. 12.
[45] *Global Volcanism Program Colima*. [Online]. Available: https://volcano.si.edu/volcano.cfm?vn=341040
[46] S. Valade *et al.*, "Towards global volcano monitoring using multisensor sentinel missions and artificial intelligence: The mounts monitoring system," *Remote Sens.*, vol. 11, no. 13, Jan. 2019, Art. no. 1528.
[47] J. D. Hunter, "Matplotlib: A 2D graphics environment," *Comput. Sci. Eng.*, vol. 9, no. 3, pp. 90–95, May 2007.
[48] *GraphPad Software*, "Graphpad prism." [Online]. Available: https://www.graphpad.com
[49] *Microsoft Corporation,* "Microsoft Excel." [Online]. Available: https://office.microsoft.com/excel

Binayak Ghosh was born in Kolkata, India. He received the B.Tech. degree in electronics and communications engineering from the Institute of Engineering and Management, Kolkata, India, in 2015 and the dual M.Sc. degrees in information and communications technology from the Technical University of Berlin, Berlin, Germany, in 2017, and the KTH Royal Institute of Technology, Stockholm, Sweden.

Since 2018, he has been working toward the Ph.D. degree with the GFZ German Research Center for Geosciences, Potsdam, Germany, with focus on application of machine learning and deep learning on SAR interferometry for natural hazard assessment.

He is part of the first cohort of the HEIBRiDS Research School, Berlin, Germany. His current research interests include the intersection of machine learning, deep learning, data science, and radar remote sensing.

Mahdi Motagh was born in Tehran, Iran, in 1975. He received the B.Sc. degree in surveying engineering and the M.Sc. degree in geodesy from the University of Tehran, Tehran, Iran, in 1998 and 2002, respectively, and the Ph.D. degree in earth sciences from the University of Potsdam, Postdam, Germany, in 2007.

In 2007, he was a Postdoctoral Scientist with various departments of GFZ German Research Center for Geosciences, Potsdam, Germany, where he became a Permanent Research Staff in 2011. In 2017, he became a Professor of radar remote sensing with Leibniz University Hannover, Hanover, Germany. His research interests include the use of radar remote sensing data to investigate processes related to various types of geological phenomena and engineering applications, such as active tectonics, landslides, floods, groundwater extraction/injection, underground mining, glacier motion and ice mass change, dam stability, and anthropogenic activities in urban areas.

Mahmud Haghshenas Haghighi received the B.Sc. degree in surveying engineering from the University of Tabriz, Tabriz, Iran, in 2009, the M.Sc. degree in remote sensing from the University of Tehran, Tehran, Iran, in 2012, and the Ph.D. degree in radar remote sensing from Leibniz University Hannover, Hanover, Germany, in 2019.

His Doctoral Research focuses on local and large-scale inSAR measurement of ground surface deformation with GFZ German Research Center for Geosciences, Potsdam, Germany. After one year of Postdoctoral Research with GFZ, he is currently a Postdoctoral Researcher with the Institute of Photogrammetry and GeoInformation, Leibniz University Hannover. His research focuses on the use of radar remote sensing for natural and anthropogenic hazards and engineering applications.

Magdalena Stefanova Vassileva received the B.Eng. and M.Eng. degrees in environmental engineering from the University of Rome La Sapienza, Rome, Italy, in 2010 and 2014, respectively. Since 2018, she has been working toward the Ph.D. degree in geodetic science with the Institute of Photogrammetry and Geoinformation, Leibniz Universität Hannover, Hannover, Germany.

From 2014 to 2018, she was an Expert of remote sensing and GISwith ITHACA, Turin, Italy, a center of applied research founded in 2006 by Politecnico of Turin, Turin, Italy. Her current research interests include multitemporal SAR Interferometry for natural and anthropogenic hazard assessment.

Thomas R. Walter received the Ph.D. degree (*summa cum laude*) from the University of Kiel, Kiel, Germany, in 2002.

From 2003 to 2005, he was a Postdoctoral Researcher with the InSAR Lab, Rosenstiel School of Marine and Atmospheric Science, University of Miami, Coral Gables, FL, USA. Since 2005, he has been the Head of the Volcanology and Neotectonics Working Group, Department of the Physics of the Earth, GFZ German Research Centre for Geosciences, Potsdam, Germany. He is currently a Professor (Apl.) of volcanology and geohazards with the University of Potsdam, where he wrote his professorial thesis and also defended his habilitation in 2010. His research interests include the observation and modeling of volcano and earthquake deformation processes and source characterization, with a focus on interacting processes, such as volcano–earthquake interactions, or the relationship between flank motion and magmatism or fluid ascent.

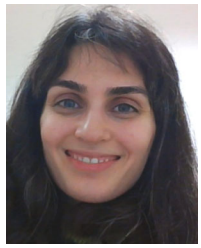

Setareh Maghsudi received the Ph.D. degree (*summa cum laude*) in computer science from the Technical University of Berlin, Berlin, Germany, in 2015.

She is currently an Assistant Professor with the University of Tübingen, Tübingen, Germany. She is also an Adjunct Lecturer with the Technical University of Berlin and a Senior Project Manager with the Fraunhofer Heinrich-Hertz-Institute, Berlin, Germany. During 2017–2020, she was an Assistant Professor with the Technical University of Berlin. During 2015–2017, she was a Postdoc with the University of Manitoba, Winnipeg, MB, Canada, and Yale University, New Haven, CT, USA. Her main research interests include the intersection of network analysis and optimization, game theory, machine learning, and data science.

She was the recipient of several competitive fellowships and career awards, including from the German Ministry of Education and Research, the German Research Foundation, and the Japan Society for the Promotion of Science.